One-step synthesis of hematite nanospindles from choline chloride/urea deep eutectic solvent with highly powerful storage versus lithium

Q.Q. Xiong, J.P. Tu[*], X. Ge, X.L. Wang, C.D. Gu

State Key Laboratory of Silicon Materials, Key Laboratory of Advanced Materials and Applications for Batteries of Zhejiang Province, and Department of Materials Science and Engineering, Zhejiang University, Hangzhou 310027, China

HIGHLIGHTS

- We prepared Fe_2O_3 nanospindles via a ionothermal strategy in the deep eutectic solvent.
- The nanospindles are assembled by nanoparticles as primary building blocks.
- The Fe_2O_3 synthesized in this strategy is firstly used as an anode material for LIBs.
- The electrode shows high capacity, good cycle stability and rate performance.

ARTICLE INFO

ABSTRACT

Fe_2O_3 nanospindles assembled with nanoparticles as primary building blocks are directly synthesized by a versatile ionothermal strategy in the choline chloride/urea mixture-based deep eutectic solvent system. The proposed ionothermal protocol is attractive and environmental friendly because choline chloride and urea are both naturally biocompatible compounds. As an anode material for lithium-ion batteries, the resultant Fe_2O_3 nanospindles show high capacity and good cycle stability (921.7 mAh g^{-1} at a current density of 200 mA g^{-1} up to 50 cycles), as well as the excellent rate capability. The good electrochemical performance can be attributed to the nanospindle structure with high sufficient interfacial contact area between the active material and electrolyte, the short diffusion distance of Li ions. The environmentally benign strategy proposed in this study is expected to offer an attractive technique for the ionothermal synthesis of electrochemical energy storage materials.

1. Introduction

Nowadays, due to the ever-growing concerns about the limited energy supplies and environment pollution, there is a greatly increased demand for green and efficient energy storage devices [1]. Lithium ion batteries (LIBs) have attracted lots of attention in both scientific and industrial fields due to their high energy density, long cycle life and good environmental benignity [2,3]. The next generation of LIBs is expected to develop superior performance in terms of capacity, cycling stability, rate capability, cost and safety to meet the demand of new emerging technologies [4]. This goal significantly relies on exploring alternative anode materials for commercial graphitic carbon that has a theoretical capacity of only 372 mA h g^{-1}, which play a key role in LIBs' electrochemical performance. Among the available anode materials, hematite (Fe_2O_3) is regarded as a potential anode material candidate for next generation LIBs due to its high theoretical capacity (1007 mA h g^{-1}), eco-friendliness, low cost, natural abundance and high resistance to corrosion [5–12].

Bulk transition metal oxides generally suffer from poor kinetics and serious capacity fade upon cycling, even at rather low rates [13]. Generally speaking, compared with bulk materials, nano-sized materials can possess distinct electrochemical properties and exhibit improved lithium storage performance arising from the large surface-to-volume ratio and small dimensions [14]. Nowadays, various types of nano-architectures have been employed as anode materials to improve the durability and high rate capability of Fe_2O_3, such as nanospindles [15], nanoflowers [16], nanoparticles [17], microspheres [18], nanorods [6], nanotubes [19] and so on.

* Corresponding author. Tel.: +86 571 87952856; fax: +86 571 87952573.
E-mail addresses: tujp@zju.edu.cn, tujplab@zju.edu.cn (J.P. Tu).

Recently, the use of ionic liquids (ILs) in inorganic synthesis has attracted increasing attention due to their particular properties of negligible vapor pressures, wide liquidus ranges, good thermal stability, tunable solubility for both organic and inorganic molecules, and much synthetic flexibility, which makes them environmentally suitable for the green chemistry [20,21]. Also ILs are a family of non-conventional molten salts that can act as templates and precursors to inorganic materials, as well as solvents [22]. Abbott and co-workers firstly described the applications of a relatively new class of ILs based on a eutectic mixture of choline chloride (ChCl) with a hydrogen bonded donor species, which is named as a deep eutectic solvent (DES) [23]. Our group has done the work about using the DES as a solvent in the electrodeposition of nanostructured metals [24–26], metal oxides [27,28] and ionothermal synthesis of nanocrystals [29,30]. However, to the best of our knowledge, the synthesis of Fe_2O_3 via one facile ionothermal route used as an anode material for LIBs has not been reported. Herein, the Fe_2O_3 nanospindles assembled with nanoparticles as primary building blocks are directly synthesized by a facile and environmentally friendly one-step synthetic route in the ChCl/urea mixture-based DES system. This Fe_2O_3 nanospindles configuration possesses the following features: high sufficient interfacial contact area between the active material and electrolyte, the short diffusion distance of Li ions, which contribute to the good electrochemical lithiation/delithiation performance of the as-prepared Fe_2O_3 nanospindles.

2. Experimental

2.1. Preparation of Fe_2O_3 nanospindles

ChCl (AR, Aladdin) and urea (AR, Aladdin) were used as received. The ChCl/urea mixture-based DES was prepared by stirring the two components in a molar ratio of 1 (ChCl): 2 (urea) at 80 °C until a homogeneous colourless liquid was formed. The DES containing 0.1 M $FeCl_3 \cdot 6H_2O$ was used as the reaction solution. After the temperature reached 200 °C, 40 ml solution was heated in a three-neck flask while it was kept under ambient atmospheric pressure by keeping the mouth open. After reaction for min, 40 ml deionized water (DIW) was quickly added into the solution with vigorous magnetic stirring. After another reaction time of 10 min, the flask was taken out and cooled rapidly in an ice bath. The black precipitate was washed with methanol and water several times and centrifuged, and finally dried at 80 °C in an oven overnight.

2.2. Characterization

The morphology and microstructure of the product was characterized by X-ray diffractometer (XRD, Rigaku D/max 2550 PC, CuKα), scanning electron microscopy (SEM, Hitachi S-4800 and FESEM, FEI Sirion-100) and transmission electron microscopy (TEM, JEM 200CX at 160 kV, Tecnai G2 F30 at 300 kV) and X-ray photoelectron spectroscopy (XPS, Thermo ESCALAB 250Xi, AlKα).

2.3. Electrochemical investigation

The electrochemical tests were evaluated using a coin-type half cell (CR 2025). The slurry consisted of 85 wt.% Fe_2O_3 nanospindles, 10 wt.% acetylene black and 5 wt.% polyvinylidene fluoride (PVDF) dissolved in N-methyl pyrrolidinone (NMP), which was then pasted on copper foil, and dried at 90 °C for 24 h in vacuum. Test cells were assembled in an argon-filled glove box with the metallic lithium foil as the counter electrode, 1 M $LiPF_6$ in ethylene carbonate (EC)-dimethyl carbonate (DME) (1:1 vol) as the electrolyte, and a polypropylene (PP) micro-porous film (Cellgard 2300) as the separator.

The galvanostatic charge–discharge measurements were conducted on a LAND battery program-control test system at various current densities over a voltage range of 0.01–3.0 V at room temperature (25 ± 1 °C). Cyclic voltammetry (CV) was performed on the CHI660C electrochemical workstation in the potential range of 0–3.0 V (vs. Li$^+$/Li) at a scanning rate of 0.1 mV s^{-1}. In the electrochemical impedance spectroscopy (EIS) measurement, the excitation voltage applied to the cells was 5 mV and the frequency range was from 100 kHz to 10 mHz. The load weight of Fe_2O_3 is about 1.25 mg cm^{-2}. The average thickness of Fe_2O_3 is about 60 μm.

3. Results and discussion

Fig. 1 reveals the XRD pattern of the collected product obtained in the ChCl/urea mixture-based DES system without further heat treatment. All the diffraction peaks can be well indexed to pure rhombohedral Fe_2O_3 (JCPDF card No. 33-0664), and the as-prepared Fe_2O_3 presents good crystallinity. The Fe_2O_3 powder is further characterized by XPS. Fig. 2 shows the Fe 2p core level XPS spectrum. Two main peaks, located at 711.0 and 724.6 eV, correspond to Fe 2p$_{3/2}$ and Fe 2p$_{1/2}$, respectively, which matches well with the reported values observed for Fe_2O_3 [31].

Fig. 3a shows a typical low magnification SEM image of the as-synthesized Fe_2O_3 powder. All the particles are uniform spindles alike. The average size of the Fe_2O_3 nanospindles is approximately 180 nm along its major axis and approximately 80 nm along its minor axis. Further observation of the Fe_2O_3 nanospindles exhibits that the surfaces of the nanospindles are rough (Fig. 3b), composed of closely packed nanoparticles as primary building blocks. Fig. 3c shows a typical TEM image of the Fe_2O_3 nanospindles, which confirms that the nanospindles are with a narrow size distribution. The relatively high-magnification TEM image in Fig. 3d shows that the tiny packed nanoparticles are with a diameter of about 5 nm. HRTEM and selected area electron diffraction (SAED) are also taken to get insight into the microstructure of the Fe_2O_3 nanospindles. Fig. 3e is the HRTEM image taken from the side of a nanospindle, in which the clear atomic lattice fringes can be seen. The distance between adjacent lattice planes is measured at about 0.25 nm, which is in good agreement with the (110) plane of Fe_2O_3. Fig. 3f presents the SAED pattern of a single nanospindle, which shows the single-crystalline nature. It is suggested that the primary nanoparticles are highly oriented, resulting in the single-crystal feature of Fe_2O_3 nanospindles.
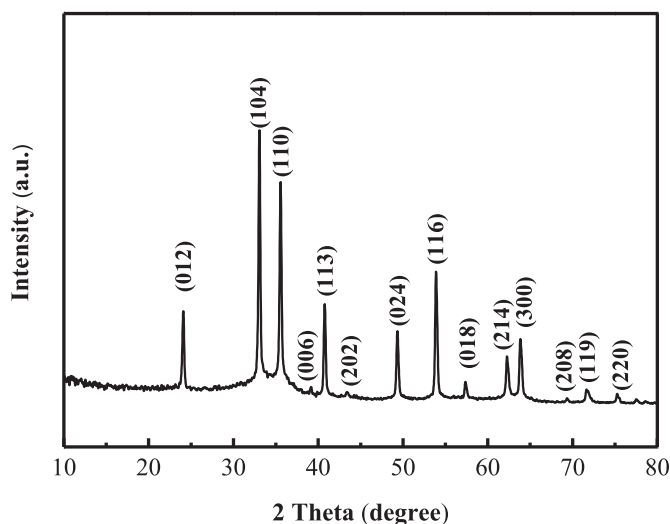

Fig. 1. XRD pattern of Fe_2O_3 nanospindles.
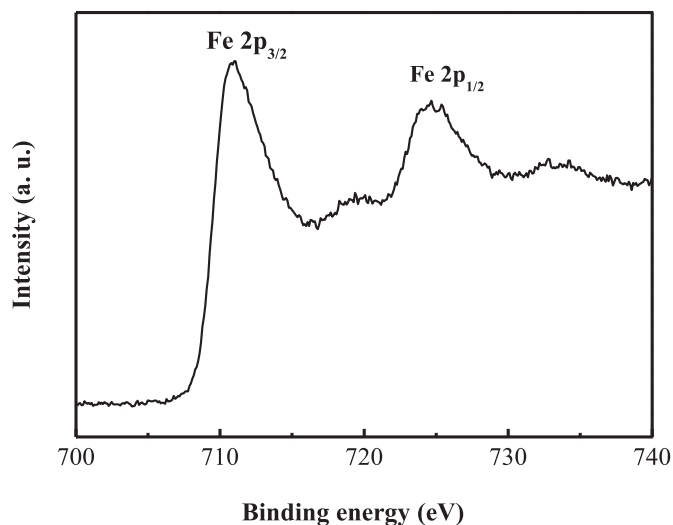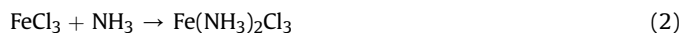
Fig. 2. XPS Fe 2p core-level spectra of Fe$_2$O$_3$ nanospindles.

According to the experimental results shown above, we propose a possible chemical reaction for the ionothermal synthesis of Fe$_2$O$_3$ nanospindles, which is described as follows:

$$CO(NH_2)_2 \rightarrow NH_3 + HCNO \tag{1}$$

$$FeCl_3 + NH_3 \rightarrow Fe(NH_3)_2Cl_3 \tag{2}$$

$$Fe(NH_3)_2Cl_3 + H_2O \rightarrow Fe_2O_3 + NH_4Cl \tag{3}$$

As the mixed Fe^{3+}/CU solution is heated under unsealed condition, the ammonia is released from the urea in DES system as shown in Eq. (1). Due to the anhydrous solution, FeCl$_3$ would react with NH$_3$. The reaction process is shown in Eq. (2) and Fe(NH$_3$)$_2$Cl$_3$ would be formed. Even though the solution changed the color to brown, the iron ion would not precipitate under this condition. After adding a small amount of DIW into the hot mixed solution, Fe(NH$_3$)$_2$Cl$_3$ could react with the H$_2$O to form Fe$_2$O$_3$ as showed in Eq. (3) and some deep brown products could precipitate out immediately. Afterward, the newly formed Fe$_2$O$_3$ nanocrystals aggregate into spindles, driven by reducing the total surface energy. During the aggregation process, the adjacent primary nanocrystals align in an orderly way by an oriented-attachment mechanism so that the particles share a planar interface in a common
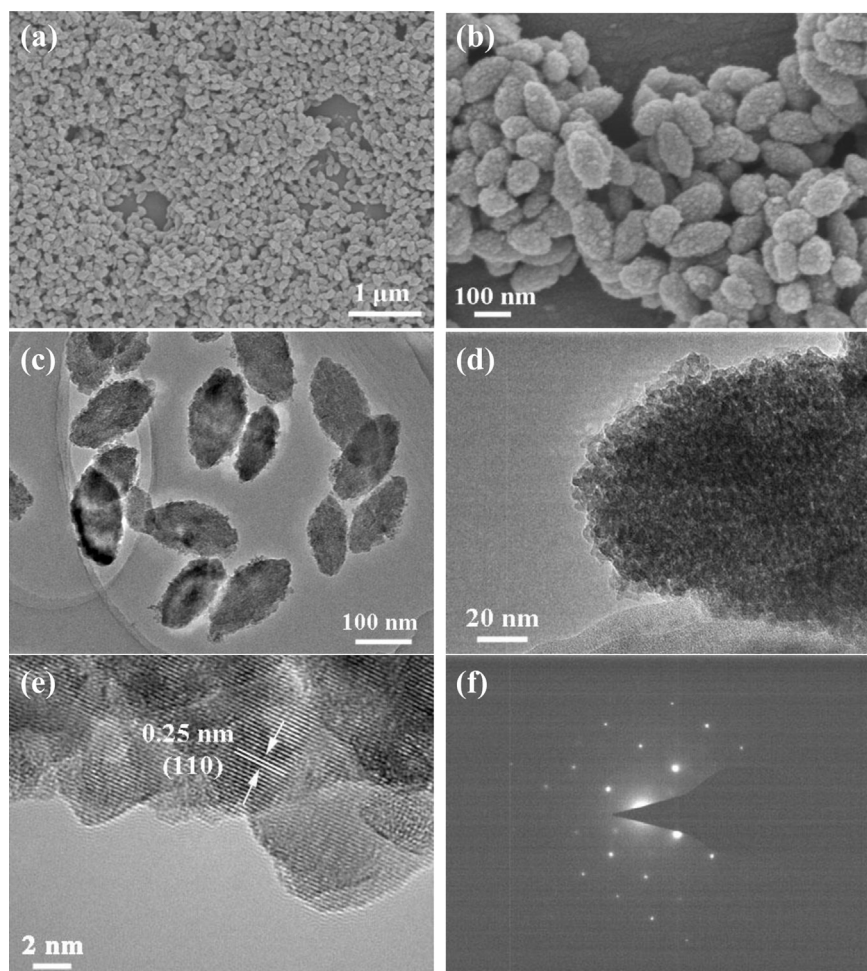

Fig. 3. (a, b) SEM images of Fe$_2$O$_3$ nanospindles; (c, d) TEM images of Fe$_2$O$_3$ nanospindles; (e) HRTEM image of Fe$_2$O$_3$ nanospindles; (f) The corresponding SAED patterns of Fe$_2$O$_3$ nanospindles.

crystallographic orientation [32]. Therefore, the formed nanospindles present a single-crystal characteristic. In our DES system, The Fe_2O_3 nanospindles assembled by tiny nanoparticles are with a narrow size distribution as shown in the histogram of the size distribution (Fig. S1), which can be attributed to the following two reasons. Firstly, the DIW was added as a reagent when the solution had already been heated to 200 °C, which resulted in a rather quick nucleation process. Secondly, the CU system has very strong hydrogen bond interactions [33]. When the DIW was added, it could be homogeneously dispersed in the solution. That could avoid the agglomeration, which would not happen in an aqueous solution. In this case, uniform Fe_2O_3 nanospindles are obtained.

In view of the potential application of Fe_2O_3 nanospindle electrode in LIBs, we investigated its ability to reversibly react with Li ions. Fig. 4a shows the CV curves of the Fe_2O_3 nanospindles from the 1st to 3rd cycle at a scan rate of 0.1 mV s^{-1} in the potential range from 0 to 3.0 V. There are two peaks, including a tiny peak at 1.5 V and an intensive one at 0.6 V, in the first cathodic scan for the Fe_2O_3 nanospindles, which can be attributed to the lithium insertion into the crystal structure of Fe_2O_3 (the formation of cubic $Li_2Fe_2O_3$) and

the reduction from Fe^{2+} to Fe^0 accompanied with irreversible decomposition reaction of electrolyte, respectively [6,34]. During the first anodic process, a broad peak is present at 1.75 V, corresponding to the reversible oxidation from Fe^0 to Fe^{3+} [19]. During the subsequent cycles, the reduction peak potential shifts to 0.8 V while the oxidation peak position is almost the same. This is due to the reduced polarization induced by small size of the electrogenerated nanograins. Importantly, the shape of CV curves in the following cycles remains similar to that of the second cycle with very small decrease in the integrated area, revealing the good reversibility of lithium storage of the Fe_2O_3 nanospindle electrode. Fig. 4b shows the first three galvanostatic charge−discharge curves for the Fe_2O_3 nanospindle electrode between 0.01 and 3.0 V at a current density of 200 mA g^{-1}. In the first discharge curve, a poorly defined plateau (1.7−0.85 V) and a perfect one at 0.8 V are clearly observed. The first plateau can be ascribed to the formation of cubic $Li_2Fe_2O_3$, and the second is attributed to the reduction from Fe^{2+} to Fe^0 and the formation of amorphous Li_2O [35], which is agreement with the above CV analysis. The two plateaus are followed by a continuous sloping curve down to the cut voltage of 0.01 V.
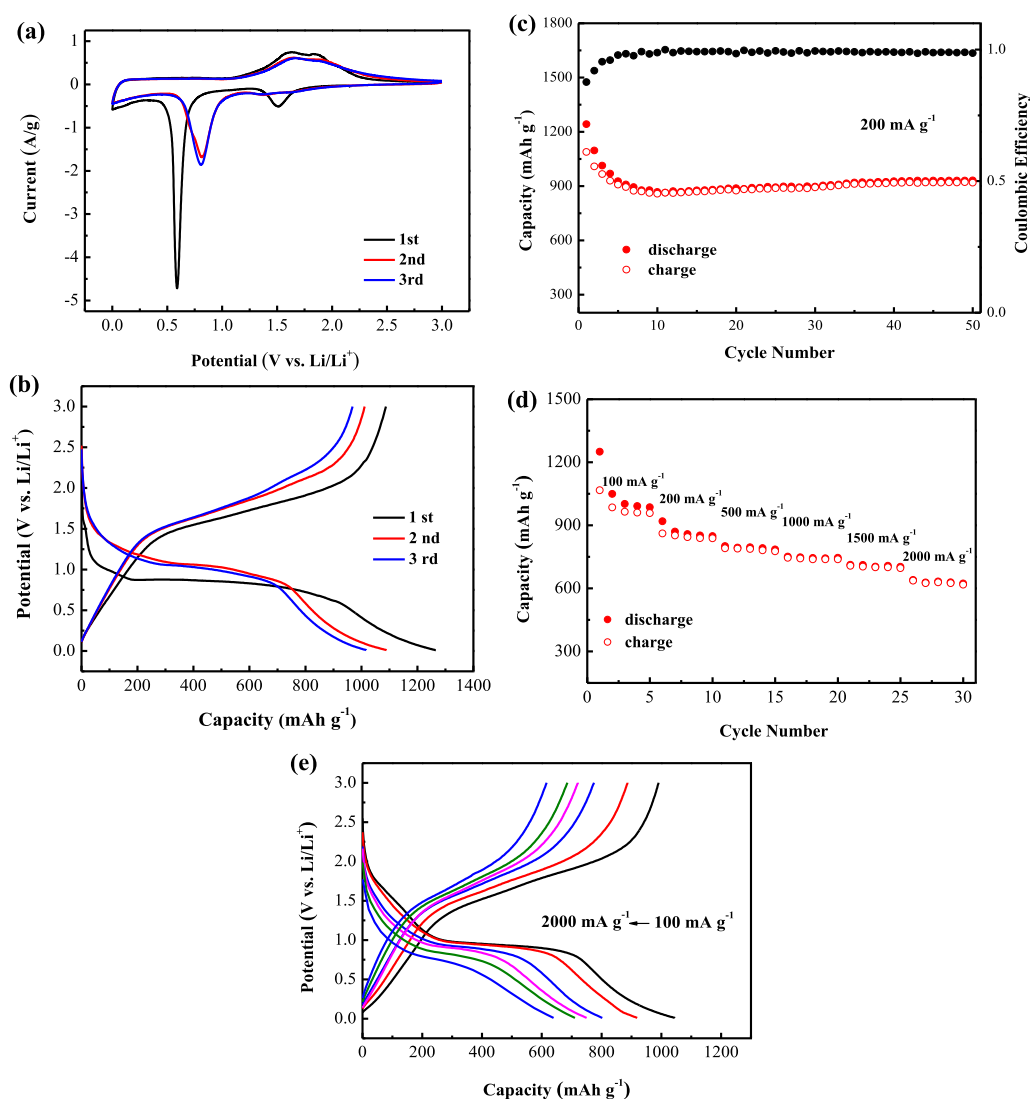
Fig. 4. (a) CV curves of Fe_2O_3 nanospindles for the first three cycles at a scan rate of 0.1 mV s^{-1} in the potential range of 0−3.0 V (vs. Li/Li$^+$); (b) Charge−discharge profiles of Fe_2O_3 nanospindles between 0.01 and 3.0 V at a current density of 200 mA g^{-1}; (c) Cycling performance of the Fe_2O_3 nanospindles at a current density of 200 mA g^{-1}; (d) Rate performance of the Fe_2O_3 nanospindles at current densities of 100 mA g^{-1} to 2000 mA g^{-1}; (e) Charge−discharge profiles of Fe_2O_3 nanospindles between 0.01 and 3.0 V at current densities from 100 mA g^{-1} to 2000 mA g^{-1}.

Previous works have concluded that reversible formation and dissolution of a gel-like film on the surface of the active oxide particles occur at low potential [36,37]. In the charging curve, since the solid electrolyte interface (SEI) film should be stable below 1.8 V, the two slopes from 1.2 to 1.8 V and from 1.8 to 3.0 V correspond to partial oxidation of Fe to intermediates, combined contribution of reversible dissolution of SEI film and the oxidation of the intermediates back to Fe_2O_3, respectively [38]. The first discharge and charge capacities are 1265.8 and 1087.3 mAh g^{-1} for the Fe_2O_3 nanospindles, corresponding to an initial columbic efficiency of 85.9%. The extra capacity compared with the theoretic capacity results from the formation of SEI film and an interfacial charging mechanism, where Li ions and electrons can be stored at the interface between electrochemically generated nanometal and Li_2O [39,40]. However, the irreversible capacity loss in the first cycle can be attributed to the formation of SEI film, the decomposition of the electrolyte and the formation of irreversible Li_2O [41,42]. Besides, during the discharge–charge process, the inherent poor electrical/ionic conductivity of the $Fe_2O_3/Fe/Li_2O$ matrix formed may also cause irreversible lithium loss [43].

The capacity versus cycle number plot of the Fe_2O_3 nanospindle electrode at the current density of 200 mA g^{-1} is shown in Fig. 4c. As can be seen, the discharge capacity decreases during the first 10 cycles, and thereafter shows an increase up to the 50th cycle and reaches 921.7 mAh g^{-1}. Such a phenomenon of the capacity increasing during cycling process has been found in many iron oxides and other transition metal oxide anode materials [44–46]. Most of the works ascribe the increasing capacity to the reversible growth of the polymeric gel-like film, which results from the kinetically activated electrolyte degradation [47,48]. It is also clear from the coulombic efficiency it is steady and higher than 99% after the 5th cycle. In addition to the good cycling performance, the Fe_2O_3 nanospindle electrode also exhibits significantly high rate capability as shown in Fig. 4d. It can be seen that the capacities are perfectly stable at the given current densities. With increasing the current density from 100 mA g^{-1} to 2000 mA g^{-1}, the discharge capacities decrease gradually, indicating the diffusion-controlled kinetics process for the electrode reaction [49]. The discharge capacities reach to 1049.0, 919.0, 800.9, 750.9 and 712.2 mAh g^{-1}, at current densities of 100, 200, 500, 1000, 1500 mA g^{-1}. Even at the current density as high as 2000 mA g^{-1}, the electrode can still deliver a capacity of 640.1 mAh g^{-1}. Fig. 4e shows the representative discharge–charge voltage profiles of the Fe_2O_3 nanospindle electrode at various current densities ranging from 100 mA g^{-1} to 2000 mA g^{-1}. When the current density increases, the overpotential of the electrode is higher with lower discharge plateau and higher charge potential, which are due to the kinetic effects of the material [50]. However, the discharge and charge curves at different current densities still keep a similar shape and the electrode delivers rather high capacity, suggesting the good rate performance of the Fe_2O_3 nanospindles. To the best of our knowledge, the Fe_2O_3 nanospindles synthesized in our experiment shows better rate retention and cycling capability than those in the published works before [18,33,34,51,52]. Compared with other transition metal oxides, even their composites, the electrochemical performance of Fe_2O_3 nanospindles is also better, like the Cu_2O [53], Co_3O_4/grapheme [54], SnO_2/Cu [55]. The good cycling performance and rate capability are attributed to the high electrochemical activity and stability of spindle nanostructure. Also the high capacity achieved at a high rate implies that this type of electrode can be a promising candidate for high power applications.

In order to further address the issue of the capacity increasing, we investigated the EIS test of the electrode at 0.01 V at the discharge state in the 2nd and 50th cycles. In this experiment, the impedance data are analyzed by fitting the equivalent electrical circuit as shown in Fig. 5a, where R_0, R_f and R_c indicate electrolyte resistance, surface film resistance and charge transfer resistance, respectively; C_f and C_d stand for the corresponding capacitances of R_f and R_c; and W represents the diffusion-controlled Warburg impedance. Herein, the R_f and C_f reflect the SEI layer whereas R_c and C_d are related to the electrochemical reaction and lithium ion diffusion in the electrode. And the former corresponds to the first semicircle in the high frequency region, while the latter to the second semicircle [56]. In Fig. 5b, the symbols are the experimental data and the continuous lines represent the fitted spectra. The Nyquist plots of the electrode in the 2nd and the 50th cycle are totally different. There is only a single broad semicircle in the high frequency region in the 2nd discharge state, while two semicircles are observed in the 50th discharge state. The difference can be attributed to the formation of the polymeric gel-like film. The formed gel-like film is an electrochemically active layer, which is swollen by the electrolyte, thus enabling ion transport to the film. For the electrochemical process, it mainly needs both ions and electrons. The reduced Fe nanoparticles can provide a conducting path for electron transport while the Li ions can come from the electrolyte once they cross the gel-like film. The resistance and capacitance of polymeric gel-like film are smaller than R_c and C_d at the beginning of the discharge–charge process, thus nothing can be found in Nyquist plots. The result confirms the growth of polymeric gel-like film with cycling and the above proposed mechanism of capacity increasing [48,57].

To further confirm the formation of the polymeric gel-like film, the electrodes were examined with TEM technique. The corresponding TEM images shown in Fig. 6 reveal a reversible formation/dissolution of the polymeric gel-like film on the surface of the Fe_2O_3 material during the discharge–charge process. Fig. 6a shows the high-magnification image near the surface of the nanoparticle after
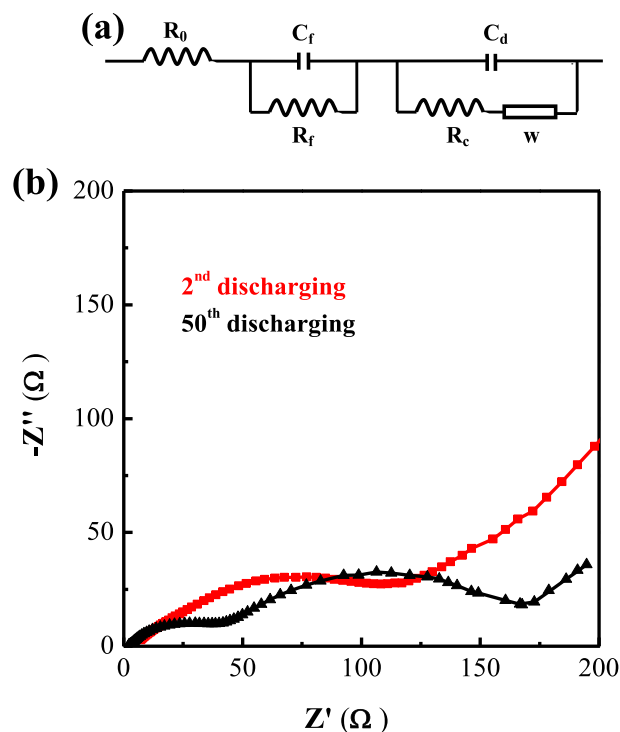

Fig. 5. (a) The equivalent circuit; (b) Nyquist plots of Fe_2O_3 nanospindle electrode at the discharge state of 0.01 V in the 2nd and 50th cycle in the frequency range from 100 kHz to 10 mHz.
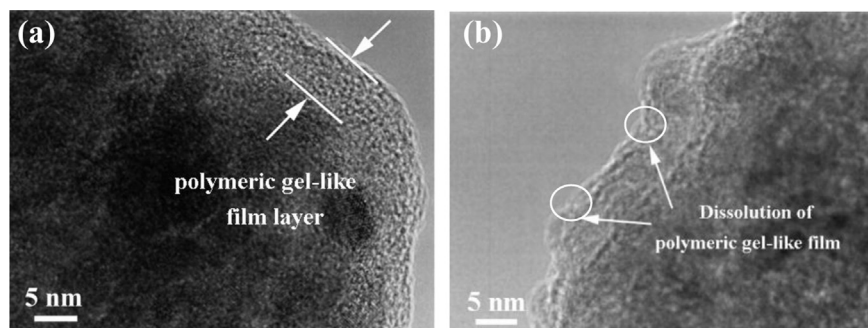
Fig. 6. TEM images of the Fe$_2$O$_3$ nanospindle after cycling: (a) after 25th discharge; (b) after 25th charge.

the 25th discharge state to 0.01 V. As can be seen, the polymeric gel-like film with a thickness of about 7 nm is formed. Two possibilities can be proposed bearing in mind that, the active materials are surrounded by the polymeric gel-like film. The first one is that the polymer film tightly binds the Fe particles ensuring an electronic conducting path with the reduced Fe nanoparticles. The second and most likely one is that the polymeric gel-like film that formed around each nanoparticle during the discharging process is a weak electronic conductor. And the polymeric gel-like film layer almost disappears after 25th full charging to 3.0 V shown in Fig. 6b. Similar results are also founded by Tarascon et al. [38,48,58]. The observation illuminates that the growth of polymeric gel-like film during cycling contributes to the increase of capacity.

4. Conclusions

In summary, we report a one-step ionothermal route to fabricate Fe$_2$O$_3$ nanospindles in the ChCl/urea mixture-based DES system. The as-prepared Fe$_2$O$_3$ nanospindles exhibit high capacity, good cycle stability (921.7 mAh g^{-1} at the current density of 200 mA g^{-1} up to 50 cycles) and high rate capability (640.1 mAh g^{-1} at the current density of 2000 mA g^{-1}) as an anode material in LIBs, due to the rather high interfacial contact area between the active material and electrolyte, short Li ion diffusion distance. The environmentally benign strategy proposed in our work is suggested as a promising method for the ionothermal synthesis of energy storage materials.

Acknowledgments

Appendix A. Supplementary data

Supplementary data related to this article can be found at http://dx.doi.org/10.1016/j.jpowsour.2014.10.020.

References

[1] A.M. Chockla, J.T. Harris, V.A. Akhavan, T.D. Bogart, V.C. Holmberg, C. Steinhagen, C.B. Mullins, K.J. Stevenson, B.A. Korgel, J. Am. Chem. Soc. 133 (2011) 20914.
[2] M. Armand, J.M. Tarascon, Nature 451 (2008) 652.
[3] P.G. Bruce, B. Scrosati, J.M. Tarascon, Angew. Chem. Int. Ed. 47 (2008) 2930.
[4] J.M. Tarascon, M. Armand, Nature 414 (2001) 359.
[5] Z.Y. Wang, D.Y. Luan, S. Madhavi, C.M. Li, X.W. Lou, Chem. Commun. 47 (2011) 8061.
[6] J.P. Liu, Y.Q. Song, S.S. Qin, Y.W. Zhang, W.Q. Gao, J. Phys. Chem. C 114 (2010) 21158.
[7] Z.Y. Wang, D.Y. Luan, S. Madhavi, Y. Hu, X.W. Lou, Energy Environ. Sci. 5 (2012) 5252.
[8] C.Y. Wu, X.P. Li, W.S. Li, B. Li, Y.Q. Wang, Y.T. Wang, M.Q. Xu, L.D. Xing, J. Power Sources 251 (2014) 85.
[9] Z.Y. Cao, B.Q. Wei, J. Power Sources 241 (2013) 330.
[10] C.T. Cherian, J. Sundaramurthy, M. Kalaivani, P. Ragupathy, P.S. Kumar, V. Thavasi, M.V. Reddy, C.H. Sow, S.G. Mhaisalkar, S. Ramakrishna, J. Mater. Chem. 22 (2012) 12198.
[11] B. Huang, K.P. Tai, S.J. Dillon, J. Power Sources 245 (2014) 308.
[12] J.J. Zhang, Y.F. Sun, Y. Yao, T. Huang, A.S. Yu, J. Power Sources 222 (2013) 59.
[13] H. Li, X.J. Huang, L.Q. Chen, Solid State Ionics 123 (1999) 189.
[14] S.L. Liu, L.N. Zhang, J.P. Zhou, J.F. Xiang, J.T. Sun, J.G. Guan, Chem. Mater. 20 (2008) 3623.
[15] W.M. Zhang, X.L. Wu, J.S. Hu, Y.G. Guo, L.J. Wan, Adv. Funct. Mater. 18 (2008) 3941.
[16] K.B. Tang, S.Y. Zeng, T.W. Li, Z.H. Liang, D. Wang, Y.K. Wang, Y.X. Qi, W.W. Zhou, J. Phys. Chem. C 112 (2008) 4836.
[17] W.J. Yu, P.X. Hou, L.L. Zhang, F. Li, C. Liu, H.M. Cheng, Chem. Commun. 46 (2010) 8576.
[18] B. Wang, J.S. Chen, H.B. Wu, Z.Y. Wang, X.W. Lou, J. Am. Chem. Soc. 133 (2011) 17146.
[19] J. Chen, L.N. Xu, W.Y. Li, X.L. Gou, Adv. Mater. 17 (2005) 582.
[20] M.J. Earle, J. Esperanca, M.A. Gilea, J.N.C. Lopes, L.P.N. Rebelo, J.W. Magee, K.R. Seddon, J.A. Widegren, Nature 439 (2006) 831.
[21] Z. Ma, J.H. Yu, S. Dai, Adv. Mater. 22 (2010) 261.
[22] A. Taubert, Z. Li, Dalton Trans. (2007) 723.
[23] A.P. Abbott, D. Boothby, G. Capper, D.L. Davies, R.K. Rasheed, J. Am. Chem. Soc. 126 (2004) 9142.
[24] Y.H. You, C.D. Gu, X.L. Wang, J.P. Tu, J. Electrochem. Soc. 159 (2012) D642.
[25] C.D. Gu, Y.H. You, X.L. Wang, J.P. Tu, Surf. Coat. Technol. 209 (2012) 117.
[26] C.D. Gu, J.P. Tu, Langmuir 27 (2011) 10132.
[27] M.L. Huang, C.D. Gu, X. Ge, X.L. Wang, J.P. Tu, J. Power Sources 259 (2014) 98.
[28] G.F. Cai, J.P. Tu, C.D. Gu, J.H. Zhang, J. Chen, D. Zhou, S.J. Shi, X.L. Wang, J. Mater. Chem. A 1 (2013) 4286.
[29] H. Zhang, Y. Lu, C.D. Gu, X.L. Wang, J.P. Tu, CrystEngComm 14 (2012) 7942.
[30] X. Ge, C.D. Gu, Y. Lu, X.L. Wang, J.P. Tu, J. Mater. Chem. A 1 (2013) 13454.
[31] T. Fujii, F.M.F. de Groot, G.A. Sawatzky, F.C. Voogt, T. Hibma, K. Okada, Phys. Rev. B 59 (1999) 3195.
[32] R.L. Penn, J. Phys. Chem. B 108 (2004) 12707.
[33] H. Sun, Y. Li, X. Wu, G.H. Li, J. Mol. Model. 19 (2013) 2433.
[34] J.P. Liu, Y.Y. Li, H.J. Fan, Z.H. Zhu, J. Jiang, R.M. Ding, Y.Y. Hu, X.T. Huang, Chem. Mater. 22 (2010) 212.
[35] M.V. Reddy, T. Yu, C.H. Sow, Z.X. Shen, C.T. Lim, G.V.S. Rao, B.V.R. Chowdari, Adv. Funct. Mater. 17 (2007) 2792.
[36] P. Balaya, H. Li, L. Kienle, J. Maier, Adv. Funct. Mater. 13 (2003) 621.
[37] H. Li, P. Balaya, J. Maier, J. Electrochem. Soc. 151 (2004) A1878.
[38] S. Laruelle, S. Grugeon, P. Poizot, M. Dolle, L. Dupont, J.M. Tarascon, J. Electrochem. Soc. 149 (2002) A627.
[39] Q.Q. Xiong, J.P. Tu, Y. Lu, J. Chen, Y.X. Yu, Y.Q. Qiao, X.L. Wang, C.D. Gu, J. Phys. Chem. C 116 (2012) 6495.
[40] A. Debart, L. Dupont, P. Poizot, J.B. Leriche, J.M. Tarascon, J. Electrochem. Soc. 148 (2001) A1266.
[41] Q.Q. Xiong, J.P. Tu, Y. Lu, J. Chen, Y.X. Yu, X.L. Wang, C.D. Gu, J. Mater. Chem. 22 (2012) 18639.
[42] J.Y. Xiang, J.P. Tu, Y.F. Yuan, X.L. Wang, X.H. Huang, Z.Y. Zeng, Electrochim. Acta 54 (2009) 1160.
[43] Y.Z. Piao, H.S. Kim, Y.E. Sung, T. Hyeon, Chem. Commun. 46 (2010) 118.
[44] P. Adelhelm, Y.S. Hu, M. Antonietti, J. Maier, B.M. Smarsly, J. Mater. Chem. 19 (2009) 1616.
[45] L. Taberna, S. Mitra, P. Poizot, P. Simon, J.M. Tarascon, Nat. Mater. 5 (2006) 567.
[46] Y.J. Fu, X.W. Li, X.L. Sun, X.H. Wang, D.Q. Liu, D.Y. He, J. Mater. Chem. 22 (2012) 17429.
[47] G.M. Zhou, D.W. Wang, F. Li, L.L. Zhang, N. Li, Z.S. Wu, L. Wen, G.Q. Lu, H.M. Cheng, Chem. Mater. 22 (2010) 5306.

[48] S. Grugeon, S. Laruelle, L. Dupont, J.M. Tarascon, Solid State Sci. 5 (2003) 895.
[49] C. Montella, J. Electroanal. Chem. 518 (2002) 61.
[50] B. Varghese, M.V. Reddy, Z. Yanwu, C.S. Lit, T.C. Hoong, G.V.S. Rao, B.V.R. Chowdari, A.T.S. Wee, C.T. Lim, C.H. Sow, Chem. Mater. 20 (2008) 3360.
[51] M.H. Wu, J. Chen, C. Wang, F.Q. Wang, B.L. Yi, W. Su, Z.F. Wei, S.N. Liu, Electrochim. Acta 132 (2014) 533.
[52] P.Y. Li, J.C. Deng, Y. Li, W. Liang, K. Wang, L.T. Kang, S.Z. Zeng, S.H. Yin, Z.G. Zhao, X.G. Liu, Y.Z. Yang, F. Gao, J. Alloy Compd. 590 (2014) 318.
[53] J.Y. Xiang, X.L. Wang, X.H. Xia, L. Zhang, Y. Zhou, S.J. Shi, J.P. Tu, Electrochim. Acta 55 (2010) 4921.
[54] B.J. Li, H.Q. Cao, J. Shao, G.Q. Li, M.Z. Qu, G. Y, Inorg. Chem. 50 (2011) 1628.
[55] W. Xu, N.L. Canfield, D.Y. Wang, J. Xiao, Z.M. Nie, J.G. Zhang, J. Power Sources 195 (2010) 7403.
[56] X.W. Li, L. Qiao, D. Li, X.H. Wang, W.H. Xie, D.Y. He, J. Mater. Chem. A 1 (2013) 6400.
[57] A. Ponrouch, M.R. Palacin, J. Power Sources 212 (2012) 233.
[58] P. Poizot, S. Laruelle, S. Grugeon, L. Dupont, J.M. Tarascon, Nature 407 (2000) 496.